

Kerr-cat Qubit Operations Below the Fault-tolerant Threshold

Bingcheng Qing^{1*†}, Ahmed Hajar^{1†}, Ke Wang^{1,2*}, Gerwin Koolstra¹, Long B. Nguyen^{1,2}, Jordan Hines¹, Irwin Huang³, Bibek Bhandari⁴, Zahra Padramrazi^{1,2}, Larry Chen¹, Ziqi Kang¹, Christian Jünger^{1,2}, Noah Goss¹, Nikitha Jain¹, Hyunseong Kim¹, Kan-heng Lee^{1,2}, Akel Hashim^{1,2}, Nicholas E. Frattini⁵, Justin Dressel^{4,6}, Andrew N. Jordan^{3,4,6,7}, David I. Santiago^{1,2}, Irfan Siddiqi^{1,2}

¹Quantum Nanoelectronics Laboratory, Department of Physics, University of California, Berkeley, CA, 94720, USA.

²Applied Mathematics and Computational Research Division, Lawrence Berkeley National Laboratory, Berkeley, CA, 94720, USA.

³Department of Physics and Astronomy, University of Rochester, Rochester, NY, 14627, USA.

⁴Institute for Quantum Studies, Chapman University, Orange, CA, 92866, USA.

⁵Department of Applied Physics and Physics, Yale University, New Haven, CT, 06520, USA.

⁶Schmid College of Science and Technology, Chapman University, Orange, CA, 92866, USA.

⁷The Kennedy Chair in Physics, Chapman University, Orange, CA, 92866, USA.

*Corresponding author(s). E-mail(s): bc.qing@berkeley.edu;
kywang@berkeley.edu;

†These authors contributed equally to this work.

Abstract

The ubiquitous noise in quantum system hinders the advancement of quantum information processing and has driven the emergence of different quantum error correction protocols. Among them, quantum error correction codes tailored for noise-biased qubits exhibit comparatively high error thresholds, making them a promising platform to achieve fault-tolerance. Nevertheless, their quantum operations are challenging and the demonstration of their performance beyond the fault-tolerant threshold remains incomplete. Here, we leverage Schrödinger cat states in scalable planar superconducting circuits to thoroughly characterize the high-fidelity single-qubit quantum operations on noise-biased qubits with systematic quantum tomography and benchmarking tools, demonstrating their state-of-the-art performance beyond the fault-tolerant threshold of the surface code. These results thus embody a transformative milestone in the exploration of quantum systems with structured noises. Notably, our framework is extensible to other structured-noise systems, paving the way for systematic characterization and validation of novel quantum platforms with structured noise.

Keywords: Fault Tolerant, Benchmarking, Noise-biased Qubit, Quantum Error Correction, Cat Qubit

1 Introduction

Rapid advancements in building quantum systems with scalable, well-characterized qubits have opened up the potential to solve problems intractable for classical computers[1–3]. However, quantum systems remain fragile, subject to various errors such as decoherence[4], dephasing[5, 6], stochastic and coherent errors[7]. As a result, quantum error correction (QEC) is essential for practical and fault-tolerant quantum computing (FTQC)[8, 9]. Most QEC protocols impose stringent performance requirements on the quantum devices due to significant hardware overhead and low error thresholds[9, 10]. The suppression of qubit error by scaling up a surface code reported in the transmon-based device (“Willow”) highlighted the progress in this direction[10]. Alternatively, tailored QEC codes explore the noise structures of quantum systems to achieve higher efficiency and error thresholds, relaxing the requirements for the quantum device performance[11–14]. QEC codes tailored for noise-biased qubits which are resilient to some of the Pauli noises, such as the repetition code[15] and XZZX surface code[16–22], have gained extensive attention. Recent work on enhancing the phase-flip lifetime of dissipative cat qubits using repetition codes marks a step toward the extreme limit where qubit noises are so strongly biased that only one error channel requires correction[15]. Nevertheless, universal gate control and quantum nondemolition readout for such qubits remain unclear[23, 24], and additional error channels beyond phase flips are still non-negligible[15]. In contrast, the exploration of Kerr-cat qubits (KCQs) with moderate noise bias has motivated the development of the XZZX surface code, which corrects general stochastic Pauli errors with higher error thresholds. Importantly, KCQs have recently been shown promising through demonstrations of their universal gate control and quantum nondemolition readout[23, 25].

In terms of implementation, the noise bias characteristics can be realized in bosonic qubits by encoding qubits into bosonic modes of quantum oscillators. Representative examples include the binomial qubits[26], Gottesman-Kitaev-Preskill (GKP) qubits[27, 28] and cat qubits[19, 23, 25, 29–37]. Among these, cat qubits, achieved by engineering Schrödinger cat states in quantum oscillators, have attracted considerable attention due to their comparatively high noise bias and low hardware complexity. Leveraging strong non-linear interactions in superconducting circuits, many theoretical proposals examined cat qubit implementations[21, 38], bias-preserving gates[39, 40], and applications in XZZX surface code for FTQC[19]. Furthermore, the observation of enhanced bit-flip lifetime of cat qubits encoded in superconducting oscillators has driven experimental advances[25, 30], including the universal gate control of KCQs[23, 41]. However, while the lifetime and gate control of noise-biased qubits have been studied, a comprehensive characterization of their noise structures remains unexplored. The reported gate fidelities are limited to around 80% to 90% due to limited device coherence and state-preparation-and-measurement (SPAM) errors[23, 25], which fall significantly short of the threshold required by many QEC codes[19, 20, 22]. Therefore, thoroughly characterizing the noise structure and obtaining SPAM-free estimations of the gate fidelities are crucial toward effectively applying noise-biased qubits in QEC[42].

In this work, we characterize the noise structure and gate performance of single-qubit operations in planar superconducting circuits for both conventional resonant-KCQ and a novel detuned-KCQ, achieving performance beyond the fault tolerant threshold of the XZZX surface code. Notably, we realize a novel detuned-KCQ with a red-detuned stabilization drive to enhance the bit-flip lifetime. While quantum operations were only reported on conventional resonant-KCQs[43–45], our results not only showcase high-fidelity universal single-qubit gate control and quantum non-demolition readout for the detuned-KCQ, but also demonstrate that its single-qubit gate performance crosses the fault-tolerance threshold of the XZZX surface code[19]. Remarkably, using gate set tomography (GST), we observe SPAM-free gate fidelities over 92% for the $X(\pi/2)$ gate and 99% for the bias-preserving $Z(\pi/2)$ gate, underscoring state-of-the-art performance. Benchmarking with \mathbb{D}_8 dihedral group randomized benchmarking (DRB)[42, 46] further reveals the noise bias exceeding 100 for noise-preserving operations. Importantly, DRB shows that the detuned-KCQ exhibits lower bit-flip errors and similar phase-flip errors compared to the resonant-KCQ, resulting in an even higher noise bias up to 250. With this enhanced noise bias, the single-qubit gate error of the detuned-KCQ goes below the fault-tolerant threshold of the XZZX surface code[19], highlighting the feasibility of QEC with detuned-KCQs. These findings position superconducting Kerr-cat qubits as strong candidates for noise-biased QEC codes, paving the way toward FTQC with noise-biased qubits.

2 Results

2.1 Noise-Biased Cat Qubit Encoding and Control

We implement the KCQ in a superconducting nonlinear oscillator by engineering its effective Hamiltonian under a strong two-photon stabilization drive. The encoding and

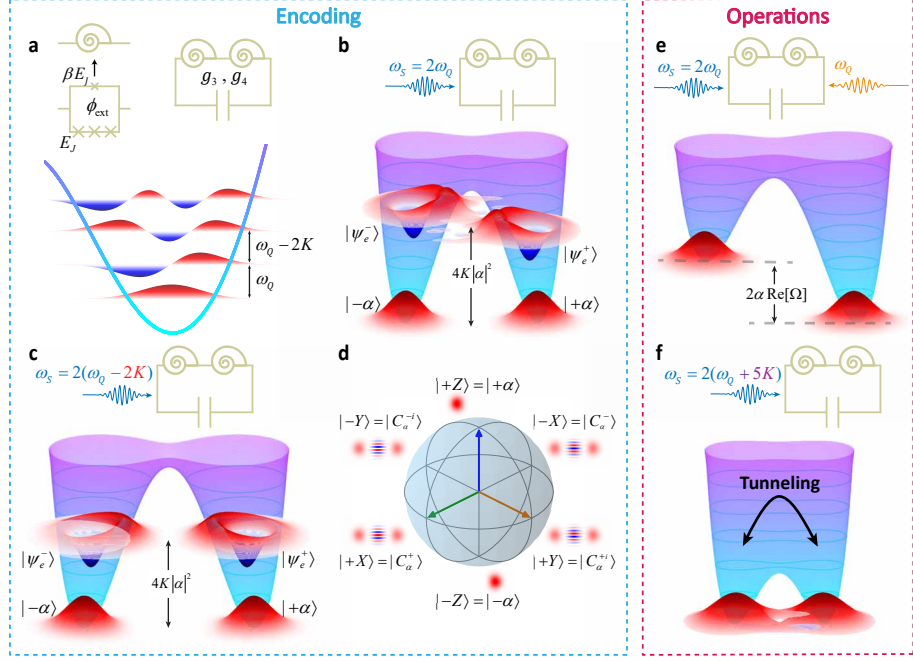


Fig. 1 Kerr-cat qubit concepts. **a** SNAIL nonlinear oscillator circuit with frequency ω_Q , nonlinear factors g_3, g_4 and Kerr nonlinearity K , and its energy levels with wave-functions. **b** SNAIL oscillator pumped by a two-photon stabilization drive at $\omega_S = 2\omega_Q$, and the engineered pseudo-potential profile with its energy levels and wave-functions. **c** Pseudo-potential profile and its energy levels engineered by a red-detuned two-photon stabilization drive, where the excited states become degenerate. **d** Bloch sphere defined by the coherent states and their superpositions, where $|\pm Z\rangle = |\pm \alpha\rangle$, $|\pm X\rangle = |C_\alpha^\pm\rangle \propto |\alpha\rangle \pm |-\alpha\rangle$, $|\pm Y\rangle = |C_\alpha^{\pm i}\rangle \propto |\alpha\rangle \pm i|-\alpha\rangle$. **e** Pseudo-potential profile under a single-photon drive Ω at ω_Q for $Z(\theta)$ gates. **f** Pseudo-potential profile under a blue-detuned two-photon stabilization drive for the $X(\pi/2)$ gate. The detuning was chosen to be $5K$ as an example.

operations of the KCQ are illustrated in Fig. 1. The nonlinear oscillator consists of two Superconducting Nonlinear Asymmetric Inductive eLements (SNAILs) shunted by a capacitor shown in Fig. 1a. Each SNAIL consists of three large Josephson junctions with Josephson energy E_J and a small Josephson junction with Josephson energy βE_J (Suppl. Info. Section 1). For a fixed external flux ϕ_{ext} , the undriven SNAIL nonlinear oscillator offers an anharmonic potential with non-zero third-order g_3 and fourth-order g_4 nonlinearities shown in Fig. 1a.

Under a two-photon stabilization drive at around twice the SNAIL oscillator frequency ($\omega_S \approx 2\omega_Q$), the effective Hamiltonian in the frame rotating at frequency $\omega_S/2$ is

$$\hat{H}_{\text{KCQ}}/\hbar = \Delta \hat{a}^\dagger \hat{a} + \epsilon_2 \hat{a}^{\dagger 2} + \epsilon_2^* \hat{a}^2 - K \hat{a}^{\dagger 2} \hat{a}^2, \quad (1)$$

where we applied the rotating wave approximation (Suppl. Info. Section 3). The detuning $\Delta = \omega_Q - \omega_S/2$ is crucial to encode the detuned-KCQ with enhanced performance. The two-photon stabilization drive ϵ_2 is engineered with the third-order nonlinearity, which converts a single photon from the drive at frequency ω_S into two photons of the SNAI oscillator at frequency ω_Q , and the Kerr coefficient K is from the fourth-order nonlinearity.

This Hamiltonian forms a pseudo-potential with a double-well structure containing two degenerate ground states at the bottom of the wells, as shown in Fig. 1b and Fig. 1c. These states are separated from the excited states $|\psi_e^\pm\rangle$ by an energy gap of $4K|\alpha|^2$ with $|\alpha|^2 = (|\epsilon_2| + \Delta/2)/K$ characterizing the cat qubit size. These ground states approach the coherent states $|\pm\alpha\rangle$ rapidly as $|\epsilon_2|/K$ increases (Suppl. Info. Section 3). By encoding these ground states as the Z -axis states on the Bloch sphere, their superposition spans the computational space of the KCQ, as shown in Fig. 1d.

As a noise biased qubit, KCQ has higher bit-flip lifetime T_z than the phase-flip lifetime T_y . The coherent states on Z axis, as eigenstates of the bosonic annihilation operator, are immune to photon losses, thus leading to the increased T_z . However, single-photon loss flips the cat states on the equator of the Bloch sphere with a rate enhanced by $|\alpha|$, leading to the reduced T_y . It is important to note that, as illustrated in Fig. 1c, the excited states are degenerate when the two-photon stabilization drive is red-detuned by $\Delta = 2K$, which leads to an even greater enhancement of the bit-flip lifetime T_z (Methods Section 4.1).

Building on our previous work of the single-qubit universal operations on a resonant-KCQ[23], we explored the single-qubit universal quantum operations on a detuned-KCQ through pseudo-potential deformation (Methods Section 4.3). The single-qubit universal gate set generally consists of continuous $Z(\theta)$ gates and an $X(\pi/2)$ gate[47]. On the one hand, by introducing a single photon drive Ω , as shown in Fig. 1e, the energies of two coherent states are shifted, resulting in a continuous $Z(\theta)$ gate. On the other hand, by blue-detuning the stabilization drive, as shown in Fig. 1f, the energy barrier between two coherent states is lowered, allowing them to tunnel between the two wells. Therefore, we can temporarily blue-detune the stabilization drive to turn on such tunneling and achieve a discrete $X(\pi/2)$ gate.

2.2 Qubit Initialization and Lifetime Characterization

The KCQ is initialized to $|+Z\rangle$ state by heralding through cat qubit readout (CQR). CQR is realized by driving the SNAI oscillator at the frequency difference with the readout resonator to engineer a beam-splitter interaction (Methods Section 4.2)[23, 25]. Under such beam-splitter interaction, the readout resonator is populated to a steady state depending on the average value of the KCQ mode $\langle\hat{a}\rangle$. Therefore, by detecting the readout resonator state, one can determine in which well the KCQ state resides, and collapse it into one of the pseudo-potential wells. This process enables the readout of KCQ along Z axis because the $|\pm Z\rangle$ states of KCQ are coherent states localized in one of the potential wells. Owing to the two-photon stabilization drive, such readout scheme is quantum nondemolition as long as the beam splitter interaction strength is much smaller than the two-photon drive strength. We achieved the

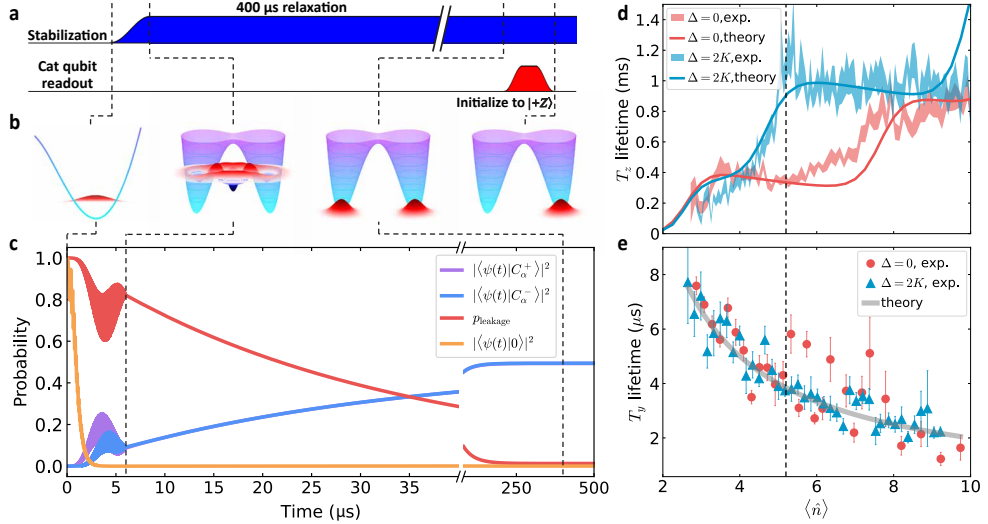


Fig. 2 Initialization and lifetimes. **a** The sequence for KCQ initialization. **b** The evolution of the potential profiles and wave-functions during the initialization. **c** The numerical simulation of the KCQ state population transfer during the initialization. **d** The bit-flip lifetime T_z of resonant-KCQ and detuned-KCQ as a function of mean photon numbers. **e** The phase-flip lifetime T_y of resonant-KCQ and detuned-KCQ. The error bars are from fitting uncertainty, and the theory predictions of the lifetimes are calculated by master-equation simulations illustrated in [37] and Methods Section 4.1.

quantum-nondemolition-ness (QNDness) over 98% which is defined as the probability of measuring the same results in two consecutive readout. Such high QNDness allows the initialization of qubits with such quantum nondemolition readout through heralding.

The initialization sequence is shown in Fig. 2a, along with the corresponding potential profiles and wave-functions in Fig. 2b. By ramping up the two-photon stabilization drive, the potential of the SNAIL oscillator is converted to a double-well pseudo-potential. Notably, due to the detuning Δ of the two-photon stabilization drive, the vacuum state may not be mapped to the ground state of the pseudo-potential. Therefore, a 400- μ s relaxation time is added to allow the state to decay to the ground states. Finally, the KCQ state is collapsed to the $|+Z\rangle$ states by heralding through CQR (Methods Section 4.3). Fig. 2c shows simulated overlaps of the KCQ state $|\psi(t)\rangle$ with the computational states $|C_\alpha^\pm\rangle = |\pm X\rangle$ and the vacuum state $|0\rangle$ during initialization with $\Delta = 2K$. The leakage out of the computational basis is defined as $p_{\text{leakage}} = 1 - |\langle\psi(t)|C_\alpha^+\rangle|^2 - |\langle\psi(t)|C_\alpha^-\rangle|^2$.

We characterize the bit-flip lifetime T_z (phase-flip lifetime T_y) of the KCQ by initializing it in Z -axis (Y -axis) and measuring the decay of the Pauli operator expectation values $\langle\sigma_z\rangle$ ($\langle\sigma_y\rangle$). As shown in Fig. 2d and Fig. 2e, T_z increases quasi-exponentially in a staircase-like manner with the mean photon number $\langle\hat{n}\rangle = |\alpha|^2$, while T_y decreases according to $T_y = T_1/(2\langle\hat{n}\rangle)$ [23], where $T_1 \approx 40$ us is the relaxation time of the SNAIL oscillator. A master equation simulation, accounting for both

single- and two-photon losses, photon heating and non-Markovian noise mechanisms, captured the behavior of T_z , with discrepancies at high $\langle \hat{n} \rangle$ mainly due to increased thermal population (Methods Section 4.1).

Due to the degeneracy of higher excited states, we observed increased T_z with detuning $\Delta = 2K, 4K, \dots$ (Methods Section 4.1). Specifically, T_z is higher for $\Delta = 2K$ compared to $\Delta = 0$ with the same mean photon number, and more importantly, the same T_y , as shown in Fig. 2d and 2e. Therefore, a detuned-KCQ with $\Delta = 2K$ is expected to exhibit greater noise bias without additional phase-flip errors, which motivates the exploration of detuned-KCQ for enhanced performance[43, 44].

In the following sections, we focus on the case where $\langle \hat{n} \rangle = 5.2$ (dashed lines in Fig. 2d and 2e) and fix the detuning of the detuned-KCQ to be $2K$. At this operating point, the T_z is large enough to provide noise bias and peaks for detuned-KCQ, and the T_y remains adequate for quantum gate control. The T_z of detuned-KCQ reaches up to 1.2 ms, approximately three times the 0.38 ms observed for the resonant-KCQ. Meanwhile, the T_y is around 4 μ s for both the resonant-KCQ and detuned-KCQ.

2.3 Gate Fidelity Characterization

To estimate the performance of gate operations on resonant-KCQ and detuned-KCQ, we implement GST to extract the error rates, gate fidelities, and SPAM-free Pauli transfer matrices (PTMs) (Suppl. Info. Section 5). The error channels are considered as a combination of coherent and stochastic Pauli errors, described by the PTM $\mathcal{E} = e^{\mathbf{L}}$. The error generator \mathbf{L} is defined as

$$\mathbf{L} = h_x \mathbf{H}_x + h_y \mathbf{H}_y + h_z \mathbf{H}_z + p_x \mathbf{P}_x + p_y \mathbf{P}_y + p_z \mathbf{P}_z, \quad (2)$$

where $\mathbf{H}_x(\mathbf{P}_x), \mathbf{H}_y(\mathbf{P}_y), \mathbf{H}_z(\mathbf{P}_z)$ are the coherent (stochastic) error generators with respect to X, Y and Z axis and $h_x (p_x), h_y (p_y), h_z (p_z)$ are the corresponding errors (Suppl. Info. Section 7).

The model violation of GST under completely positive, trace preserving (CPTP) constraints is as small as $N_\sigma = 14.51$, indicating the validity of the model. The SPAM-free estimation of the PTMs, errors and fidelities for $X(\pi/2)$ and $Z(\pi/2)$ gates are shown in Fig. 3. For $Z(\pi/2)$ gates, the stochastic Pauli X and Y errors are significantly smaller than the stochastic Pauli Z errors, confirming the bias preservation. Our KCQs have low coherent errors, as indicated by the similar diamond distances and process infidelity. In fact, the effects of coherent errors are negligible after Pauli twirling and have no statistically observable effects on the XZZX surface code error threshold (Suppl. Info. Section 7). According to the extracted process infidelities of the quantum gates, the process fidelities of $Z(\pi/2)$ and $X(\pi/2)$ gates for resonant-KCQ are 99.3% and 94.7%, and the detuned-KCQ has similar performance with the fidelities of 99.2% and 92.5%, respectively, signifying state-of-the-art performance[23, 25].

2.4 Noise Bias Characterization

The quantum operations usually introduces additional noises, which may degrade the noise bias. Therefore, it is essential to benchmark the noise bias of bias-preserving

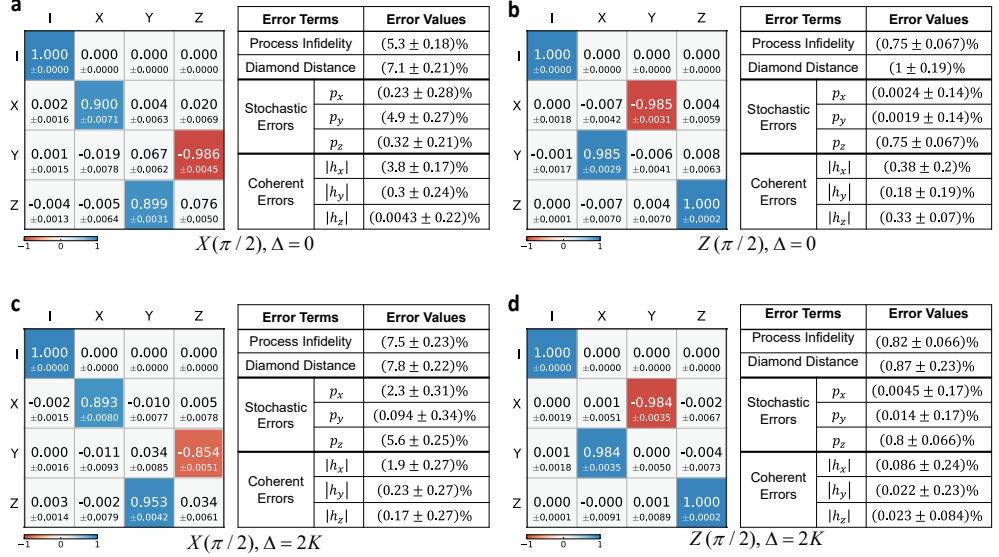


Fig. 3 GST results. SPAM-free Pauli transfer matrices, process infidelities, diamond distances, stochastic Pauli errors and coherent Pauli errors for **a** resonant-KCQ $X(\pi/2)$ gate with 367-ns gate time, **b** resonant-KCQ $Z(\pi/2)$ gate with 70-ns gate time, **c** detuned-KCQ $X(\pi/2)$ gate with 418-ns gate time and **d** detuned-KCQ $Z(\pi/2)$ gate with 70-ns gate time. The uncertainty represents the standard deviation of the model fitting.

gate sets on KCQ. Based on the stochastic Pauli error channel, we define the bit-flip error as $p_{\text{bit}} = p_x + p_y$, the phase-flip error as $p_{\text{ph}} = p_z$ and the noise bias as $\eta = p_{\text{ph}}/p_{\text{bit}}$. We present the first experimental application of DRB protocol on the KCQ to extract the noise structure of the $Z(\theta)$ gates with high precision[42, 46]. This protocol is also extensible to multi-qubit gate benchmarking by a recent protocol on CX dihedral groups[42].

The single-qubit \mathbb{D}_8 dihedral group is generated by $X(\pi)$ and $Z(\pi/4)$ gates. The $X(\pi)$ gate for KCQ is trivially a π phase shift of the reference, which can be applied virtually by adding an extra phase to the following control and readout pulses in a noise-free manner. This noise-free virtual $X(\pi)$ gate generates a bias-preserving \mathbb{D}_8 dihedral group with $Z(\pi/4)$ gates, allowing the extraction of bit-flip and phase-flip error separately. However, the noise-free property of the virtual $X(\pi)$ gate leads to underestimation of the extracted errors of $Z(\theta)$ rotations because the extracted errors are weighted averages of both noise-free virtual $X(\pi)$ gate and noisy $Z(\theta)$ rotations. To address such underestimation, scaling factors of 1.07 for p_{bit} and 1.02 for p_{ph} derived from numerical simulations are introduced (Suppl. Info. Section 6). As a result, by applying the DRB protocol, we can extract the bit-flip errors, phase-flip errors, and the noise bias of the bias-preserving gates precisely.

We explore the noise structure of the resonant-KCQ and detuned-KCQ as a function of $Z(\theta)$ gate times, with results shown in Fig. 4a, where the uncertainty of the

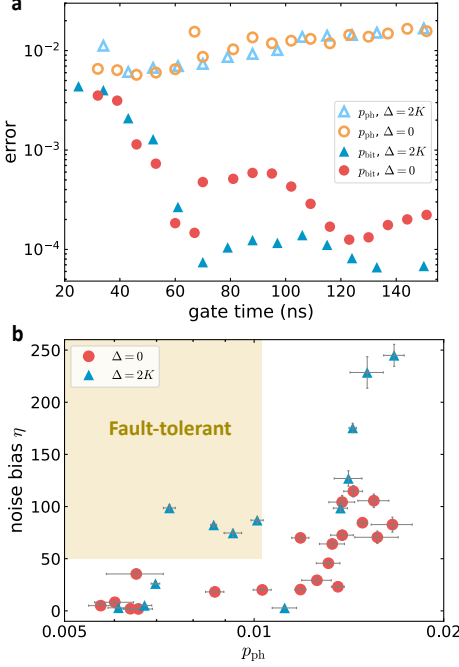


Fig. 4 DRB results. **a** The bit-flip p_{bit} and phase-flip p_{ph} error of resonant- and detuned-KCQ. The error bars are smaller than the marker size and therefore not plotted. **b** The noise bias and phase-flip error on the same plot with the fault-tolerant regime shaded in yellow. The error bars indicate the fitting uncertainty of the DRB survival probability.

extracted errors is significantly smaller than that from GST. For both the resonant-KCQ and detuned-KCQ, the bit-flip error is much lower than the phase-flip error. The bit-flip error increases when the gate time is short because the strong gate pulses introduce leakage into the higher excited states, which increases the likelihood of tunneling between the two wells of the pseudo-potential. Conversely, the phase-flip error increases when the gate time is long due to the limited phase-flip lifetime. Interestingly, several local minima in the bit-flip error are observed, potentially linked to detailed leakage mechanisms and offering insights into optimal gate time determination.

For gate times longer than 60 ns, where the leakage mechanism is not dominant, the detuned-KCQ has a lower bit-flip error than the resonant-KCQ while maintaining the same phase-flip error, which directly demonstrates the advantage of the detuned-KCQ. Within a large range of gate times, we can achieve a noise bias as high as 100 for resonant-KCQ and 250 for detuned-KCQ with a reasonable phase-flip error rates below 2%, as shown in Fig. 4b. According to the previous work, with the tailored XZZX surface code, such noise bias can lead to 50% improvement of the error threshold with standard CX gates[19].

We proceed to assess the feasibility of using KCQ for QEC. Previous studies reported that the XZZX surface code has an error threshold of $p_{\text{ph}} < 0.98\% \pm 0.05\%$ with a noise bias $\eta \geq 50$ [19]. Accordingly, we show the phase-flip error for different

noise bias η in Fig. 4b, with the fault tolerant region shaded in yellow. Above all, the detuned-KCQ demonstrates performance well within the fault tolerant region when the $Z(\theta)$ gate duration is between 70 ns to 97 ns, as indicated by the four points inside the fault tolerant region.

3 Discussion

In summary, we have characterized and benchmarked high-fidelity quantum operations on a noise-biased KCQ within a scalable planar superconducting architecture. By introducing a novel detuned stabilization drive to enhance the bit-flip lifetime, we demonstrate the first implementation of quantum nondemolition readout and high-fidelity single-qubit universal quantum operations on a detuned-KCQ, achieving performance crossing the fault-tolerant threshold of the XZZX surface code[19]. Using GST, we measure SPAM-free gate fidelities of over 92% for the $X(\pi/2)$ gate and 99% for the bias-preserving $Z(\pi/2)$ gate, representing the highest performance reported in this field. The noise bias characteristic is implied in the enhanced bit-flip lifetime and directly examined through the DRB protocol. Remarkably, the detuned-KCQ exhibits a bit-flip lifetime of $T_z \approx 1.2$ ms, with a phase-flip lifetime comparable to the resonant-KCQ counterpart. This results in a noise bias as high as 250, which is crucial for surpassing the error threshold of the XZZX surface code[19]. The device's performance is primarily limited by the relaxation rate of the SAIL oscillator, which can be mitigated through material improvement[48]. Further performance gains can be achieved by speeding up gate operations via pulse shaping[49, 50] and through optimized circuit designs[37].

Our work exemplifies the characterization and benchmarking of noise-biased qubits, providing a framework that can be extended to other bosonic systems with structured noises, such as dissipative cat qubits[15, 30], GKP qubits[27, 28, 51] and binomial qubits[26]. Compared to other bosonic qubit platforms with biased noise, the detuned-KCQ uniquely achieves high-fidelity quantum nondemolition readout and universal gate operations simultaneously with low hardware complexity. It is also compatible with recently demonstrated two-qubit gate operations in experiment[52]. Leveraging a scalable planar superconducting architecture, our work is well-positioned for extension into multi-qubit processors, paving the way for the application of noise-biased qubits in QEC and FTQC. Moreover, the enhanced bit-flip lifetime of the detuned-KCQ presents it a promising ancilla for universal control of a quantum cavity, effectively mitigating parasitic error propagation[53, 54]. As a Kerr parametric oscillator (KPO) with the double-well potential, the detuned-KCQ also opens new possibilities for KPO-network-based Ising machines, fostering advancements in analog quantum computing[55–57].

4 Methods

4.1 Master Equation Simulation of Coherent State Lifetimes

We illustrate the simulation of coherent state lifetimes T_z in this section and emphasize the enhancement of coherent state lifetimes when the two-photon stabilization drive is detuned by $2K, 4K...$ due to the degenerate higher excited states.

The Kerr-cat qubit inevitably disperses irretrievable information to the environment, leading to incoherent processes. We model the environment by a chain of harmonic oscillators with infinite modes and temperature T_E . While the exact dynamics of arbitrary system-environment interaction and environment evolution is intractable analytically, one can construct the master equation describing various effects of the environment on the system under assumptions that generally hold in the experiments, including weak system-environment coupling and a Markovian thermal environment. For simplicity, we consider a environment with fixed thermal distribution and energy-independent coupling with the system. With the above approximations, the master equation has the following form

$$\frac{d\hat{\rho}}{dt} = -i[\hat{H}, \hat{\rho}] + \sum_l \gamma_l \mathcal{D}[\hat{O}_l]\hat{\rho}, \quad (3)$$

where \hat{O}_l describe three sets of incoherent processes, including $\hat{O}_{1,\downarrow} (\hat{O}_{1,\uparrow}) = \hat{a} (\hat{a}^\dagger)$ for the single-photon dissipation (excitation) process, $\hat{O}_{2,\downarrow} (\hat{O}_{2,\uparrow}) = \hat{a}^2 (\hat{a}^{\dagger 2})$ for the two-photon dissipation (excitation) process, and $\hat{O}_\phi = \hat{a}^\dagger \hat{a}$ for the dephasing process. The corresponding coefficients $\gamma_{1,\downarrow} (\gamma_{1,\uparrow}) \propto \kappa^{(1)}$, $\gamma_{2,\downarrow} (\gamma_{2,\uparrow}) \propto \kappa^{(2)}$, and $\gamma_\phi \propto \kappa_\phi$ are single-photon dissipation (excitation), two-photon dissipation (excitation), and dephasing rates, where $\kappa^{(1)}$ and $\kappa^{(2)}$ are the single-photon and two-photon spontaneous decay rates, respectively. A detailed derivation of the master equation along with the expressions for $\gamma_{1,\downarrow} (\gamma_{1,\uparrow})$, $\gamma_{2,\downarrow} (\gamma_{2,\uparrow})$ and γ_ϕ is presented in references[23, 37, 58]. Beyond the three incoherent processes above, we also consider a stochastic process that leads to fluctuations in the SNAI nonlinear oscillator frequency with a noise strength of ξ [23, 37].

The experimental behavior of the coherent state lifetimes T_z is accurately modeled by such four processes in a thermal environment with thermal photon population $n_{th} = 5\%$, as shown by the agreement between the experiment data and master equation simulation results in Fig. 2. Here, we illustrate the effects of each process in detail. As shown in Fig. 5a, we fit the coherent state lifetimes of a resonant-KCQ as a function of two-photon stabilization drive strength ϵ_2 . When only considering the single-photon dissipation and excitation, i.e. $\kappa^{(2)} = \kappa_\phi = \xi = 0$, the master equation simulation follows the blue curve, overestimating the coherent lifetimes. By introducing the stochastic frequency fluctuation of the SNAI nonlinear, i.e. $\kappa^{(2)} = \kappa_\phi = 0$, the master equation simulation successfully modeled the coherent state lifetimes with small ϵ_2 following the yellow curve, but failed to model the strongly driven regime. Finally, only by including all four processes, the master equation simulation accurate models the experiment data, as shown by the red curve.

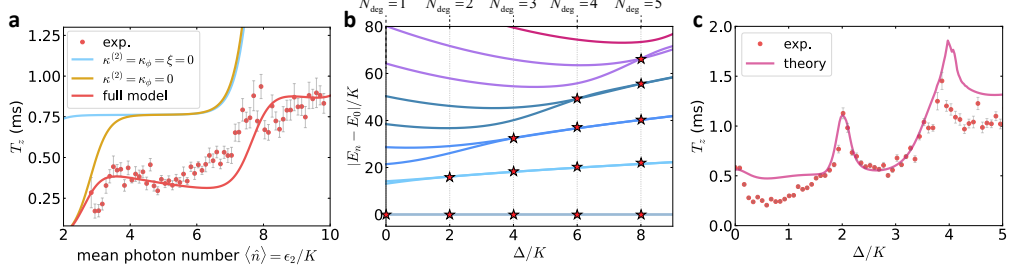


Fig. 5 Master equation simulation. **a** The coherent state lifetimes with different mean photon number and their master equation simulation taking different incoherent processes into account. **b** KCQ Hamiltonian spectrum with detuned two-photon stabilization drive. **c** The coherent state lifetimes with different detuning and their master equation simulation.

Beyond the influence on coherent state lifetimes by the two-photon stabilization drive strength, the detuning of two-photon stabilization drives, with $\Delta = 2K, 4K, \dots$, can lead to degenerate higher excited states marked by the stars in Fig. 5b, and increase the coherent state lifetimes. We observe N_{deg} degenerate points, corresponding to $N_{\text{deg}} - 1$ higher excited degenerate states, when $\Delta = 2(N_{\text{deg}} - 1)K$. With a fixed two-photon stabilization drive strength $\epsilon_2 = 4.2K$, we measured the coherent state lifetimes with various detuning Δ , as shown in Fig. 5c. The increase of the coherent state lifetime when $\Delta = 2K$ and $4K$ is both observed in experimental data and predicted in the master equation simulations, demonstrating the validity of the theoretical model.

4.2 KCQ Readout

The readout of the KCQ is enabled by a beam-splitter interaction between the KCQ mode \hat{a} and the readout resonator mode \hat{b} , driven at their frequency difference. By applying a cat-qubit-readout (CQR) drive at frequency $\omega_{CQR} = \omega_R - \omega_S/2$, we can engineer a beam-splitter interaction enabled by the third order nonlinearity of the SAIL, as depicted in

$$\hat{H}_{BS} = \epsilon_{CQR} a^\dagger b + \epsilon_{CQR}^* a b^\dagger, \quad (4)$$

where ω_R is the readout resonator frequency and ϵ_{CQR} is the interaction rate.

Such an interaction will populate the readout resonator mode \hat{b} into two different states[25] depending on the expectation value of the KCQ mode \hat{a} as

$$\langle \hat{b} \rangle(t \rightarrow +\infty) = \frac{2\epsilon_{CQR}}{\kappa_R} \langle \hat{a} \rangle, \quad (5)$$

where κ_R denotes the the decay rate of the readout resonator. Therefore, by detecting the state of the readout resonator, we can determine in which well of the pseudo-potential the KCQ resides, corresponding to a readout along Z axis when KCQ states remain in the computational basis. This readout scheme is quantum-nondemolition when the photon swap rate between the KCQ and readout resonator is far lower than the two-photon stabilization strength, i.e. $\epsilon_{CQR} \ll \epsilon_2$.

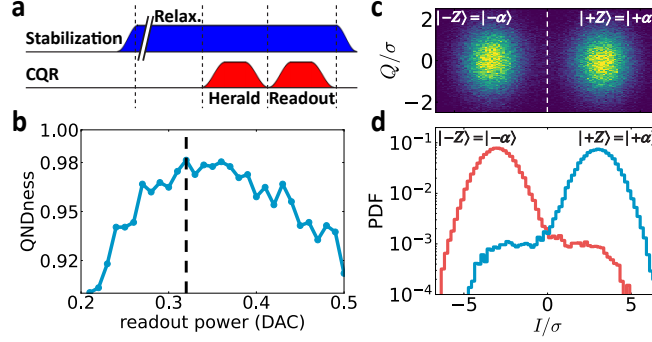


Fig. 6 CQR calibration. **a** The pulse sequence to calibrate the quantum nondemolition readout. **b** The QNDness with various CQR drive strength, with zoomed in view around high QNDness region as an inset. **c** The histogram of the readout output when preparing the states in a thermal mixture of $|\pm Z\rangle$. **d** The histogram of the readout output when preparing the states in either $|+Z\rangle$ (orange) or $| -Z\rangle$ (blue).

The readout calibration sequence is shown in Fig. 6a, where the stabilization drive is turned on, followed by a long relaxation period ($\sim 400 \mu\text{s}$) to allow the states to decay back to the computational basis. Two $4.5\text{-}\mu\text{s}$ CQR drives labeled as ‘‘Herald’’ and ‘‘Readout’’ are then applied sequentially. The QNDness is defined as $(P[M_{|+\alpha}\rangle|M_{|+\alpha}\rangle] + P[M_{|-\alpha}\rangle|M_{|-\alpha}\rangle])/2$, where $P[M_A|M_B]$ represents the probability of getting result A with the ‘‘Readout’’ pulse conditioned on having obtained result B with the ‘‘Herald’’ pulse. The QNDness is optimized for different CQR drive strengths and the optimized readout strength, indicated by the dashed line in Fig. 6b, resulting in good separation of the two readout blobs with the corresponding histogram shown in Fig. 6c and Fig. 6d.

4.3 KCQ Universal Gate Control and Initialization

The single qubit universal gate set of the KCQ consists of a discrete $X(\pi/2)$ gate and continuous $Z(\theta)$ rotation gates, which are implemented by the deformation of the double-well pseudo-potential profile. The $X(\pi/2)$ gate, corresponding to the coherent tunneling between the two wells of the pseudo-potential, is realized by adiabatically lowering the energy barrier between the two wells. As illustrated in our previous work[23], we realize such gate by phase-modulating the two-photon stabilization drive $\epsilon_2(t) = \epsilon_2(0)e^{-ig(t)}$ with $g(t)$ defined as

$$g(t) = \delta_0 t \times \begin{cases} -\sin\left(\frac{3\pi}{2}t/T_g\right) & t \leq T_g/3 \\ -\frac{f(t)}{1-f(T_g)}(f(t) - f(T_g)) & t > T_g/3, \end{cases} \quad (6)$$

where T_g is the gate time, δ_0 is the modulation depth, and $f(t) = \exp\left(-\frac{8(t-T_g/3)^2}{T_g^2}\right)$ follows a Gaussian profile. Such phase modulation adiabatically introduces a blue-detuning to the two-photon stabilization drive and correspondingly, lower the energy barrier of the pseudo-potential to allow the inter-well tunneling, as shown in Fig. 7c.

We calibrate the $X(\pi/2)$ gate with the sequence shown in Fig. 7a. A CQR pulse (labeled ‘‘Herald’’) initializes the qubit into $|+Z\rangle$ state through heralding. Then,

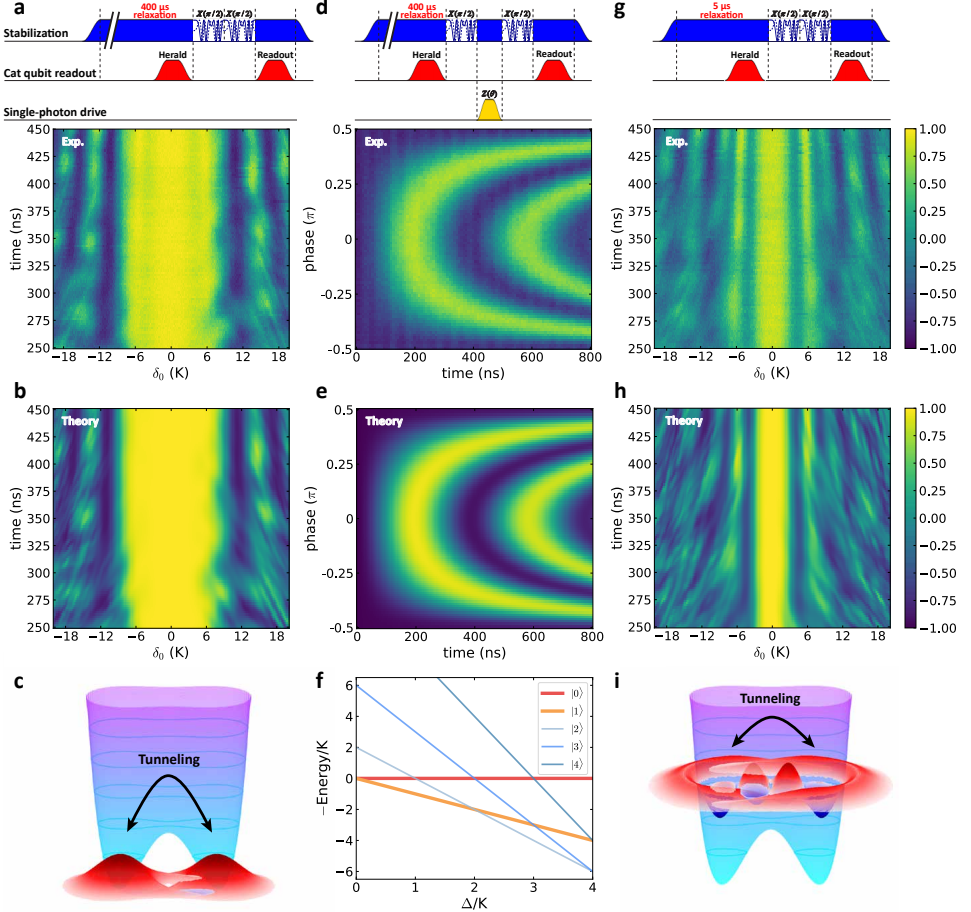


Fig. 7 KCQ initialization and gate calibration. **a** The sequence for calibrating $X(\pi/2)$ gate with 400- μ s relaxation time in the initialization, and the measured $|\pm Z\rangle$ population oscillation. **b** The numerical simulation of the results above it. **c** The tunneling between the ground states when the relaxation time is long enough in the initialization. **d** The sequence for calibrating $Z(\theta)$ gates and the measured Chevron-like plot. **e** The numerical simulation of the results above it. **f** The energy levels of the SNAIL nonlinear oscillator modified by the detuning. **g** The sequence for observing the excited states tunneling with 4- μ s relaxation time in initialization, and the measured population oscillation. **h** The numerical simulation of the results above it. **i** The tunneling between the excited states when the relaxation time is short.

two $X(\pi/2)$ gate pulses with various modulation depth δ_0 and duration are applied. Finally, another CQR pulse (labeled “Readout”) is applied to readout the qubit state. The measured expectation of the Pauli Z operator $\langle \hat{\sigma}_z \rangle$ is shown in Fig. 7a, which clearly shows population oscillating coherently between the $|\pm Z\rangle$ states. The numerical simulation, based on solving the time-dependent Schrödinger equations, is shown in Fig. 7b in good agreement with the experimental results. Therefore, we calibrate the $X(\pi/2)$ gate for KCQs by optimizing the gate time and the modulation depth to achieve the largest $\langle \hat{\sigma}_z \rangle$ conversion.

The $Z(\theta)$ gates are realized by a single-photon drive at frequency $\omega_S/2$, which introduces a Hamiltonian $\hat{H}_d = \hat{a}^\dagger\Omega/2 + \hat{a}\Omega^*/2$. Such Hamiltonian leads to an energy difference of $2\text{Re}[\Omega]\alpha$ between the $|\pm Z\rangle$ states and results in a Rabi oscillation on the equator of the Bloch sphere. We calibrate $Z(\theta)$ gates following the pulse sequence shown in Fig. 7d. The pre-calibrated $X(\pi/2)$ gates are used to prepare and measure the state along Y axis. The phase and duration of the single-photon drive are swept to obtain the Chevron-like plot shown in Fig. 7d, which is in good agreement with the numerical simulation shown in Fig. 7e. Importantly, for both quantum operations, a large enough relaxation time ($400\ \mu\text{s}$) is necessary for the initialization of the qubit and we will discuss about this in the following.

The initialization of the KCQ is implemented through the CQR pulse by heralding. The SNAIL nonlinear oscillator mode predominantly remains in the vacuum state $|0\rangle$ with neglectable thermal noise at low temperature. Therefore, the resonant-KCQ can be initialized by adiabatically ramping up the two-photon stabilization drive followed by a CQR drive, which maps the vacuum state to the cat state and then collapses it into $|\pm Z\rangle$. However, this technique fails for the detuned-KCQ because the finite detuning changes the energies of SNAIL nonlinear oscillator states in the rotating frame. As shown in Fig. 7f, a finite Δ alters the spectrum in the rotating frame, causing $|0\rangle$ no longer be the ground state, while the cat states remain the ground states of the KCQ Hamiltonian. Consequently, when the two-photon stabilization drive is ramped up, the $|0\rangle$ state is mapped to the higher excited states instead of the ground states. The subsequent CQR drive will then collapse the qubit into excited states in one of the double wells of the pseudo-potential, resulting in a failure to initialize the qubit into $|\pm Z\rangle$ states. To address this, it is crucial to introduce sufficient relaxation time before applying the CQR drive, allowing the system to decay into the degenerate ground states. This ensures the validity of preparing the $|\pm Z\rangle = |\pm\alpha\rangle$ state through heralding.

To observe the effect of higher excited states, we applied a sequence similar to that used for calibrating the $X(\pi/2)$ gate to a detuned-KCQ system with $\Delta = 2K$, but with the relaxation time reduced to $5\ \mu\text{s}$, as shown in Fig. 7g. Due to this shortened relaxation time, the detuned-KCQ states predominantly occupy the excited states, and the pulse sequence captures the population oscillation between these excited states within each well, as illustrated in Fig. 7i. The experimental results, presented in Fig. 7g, show a reduced contrast and tunneling occurring at a lower modulation depth. The numerical simulation of the excited state dynamics aligns perfectly with the experimental observations.

References

- [1] Shor, P. W. Polynomial-time algorithms for prime factorization and discrete logarithms on a quantum computer. *SIAM review* **41**, 303–332 (1999).
- [2] Arute, F. *et al.* Quantum supremacy using a programmable superconducting processor. *Nature* **574**, 505–510 (2019).
- [3] Zhong, H.-S. *et al.* Quantum computational advantage using photons. *Science* **370**, 1460–1463 (2020).

- [4] Martinis, J. M. *et al.* Decoherence in josephson qubits from dielectric loss. *Phys. Rev. Lett.* **95**, 210503 (2005).
- [5] Bluvstein, D. *et al.* Logical quantum processor based on reconfigurable atom arrays. *Nature* **626**, 58–65 (2024).
- [6] Reilly, D. *et al.* Suppressing spin qubit dephasing by nuclear state preparation. *Science* **321**, 817–821 (2008).
- [7] Hashim, A. *et al.* Randomized compiling for scalable quantum computing on a noisy superconducting quantum processor. *Phys. Rev. X* **11**, 041039 (2021).
- [8] Fowler, A. G., Mariantoni, M., Martinis, J. M. & Cleland, A. N. Surface codes towards practical large-scale quantum computation. *Phys. Rev. A* **86**, 032324 (2012).
- [9] Google Quantum AI. Suppressing quantum errors by scaling a surface code logical qubit. *Nature* **614**, 676–681 (2023).
- [10] Acharya, R. *et al.* Quantum error correction below the surface code threshold. *Nature* (2024).
- [11] Michael, M. H. *et al.* New class of quantum error-correcting codes for a bosonic mode. *Phys. Rev. X* **6**, 031006 (2016).
- [12] Levine, H. *et al.* Demonstrating a long-coherence dual-rail erasure qubit using tunable transmons. *Phys. Rev. X* **14**, 011051 (2024).
- [13] Aliferis, P. *et al.* Fault-tolerant computing with biased-noise superconducting qubits: a case study. *New J. Phys.* **11**, 013061 (2009).
- [14] Wu, Y., Kolkowitz, S., Puri, S. & Thompson, J. D. Erasure conversion for fault-tolerant quantum computing in alkaline earth rydberg atom arrays. *Nat. Commun.* **13**, 4657 (2022).
- [15] Putterman, H. *et al.* Hardware-efficient quantum error correction using concatenated bosonic qubits. *preprint arXiv:2409.13025* (2024).
- [16] Tuckett, D. K., Bartlett, S. D. & Flammia, S. T. Ultrahigh error threshold for surface codes with biased noise. *Phys. Rev. Lett.* **120**, 050505 (2018).
- [17] Tuckett, D. K. *et al.* Tailoring surface codes for highly biased noise. *Phys. Rev. X* **9**, 041031 (2019).
- [18] Tuckett, D. K., Bartlett, S. D., Flammia, S. T. & Brown, B. J. Fault-tolerant thresholds for the surface code in excess of 5% under biased noise. *Phys. Rev. Lett.* **124**, 130501 (2020).

- [19] Darmawan, A. S., Brown, B. J., Grimsmo, A. L., Tuckett, D. K. & Puri, S. Practical quantum error correction with the xzzx code and kerr-cat qubits. *PRX Quantum* **2**, 030345 (2021).
- [20] Bonilla Ataides, J. P., Tuckett, D. K., Bartlett, S. D., Flammia, S. T. & Brown, B. J. The xzzx surface code. *Nat. Commun.* **12**, 2172 (2021).
- [21] Xu, Q. *et al.* Engineering kerr-cat qubits for hardware efficient quantum error correction. *SPIE* **12015**, 50–63 (2022).
- [22] Xu, Q. *et al.* Tailored xzzx codes for biased noise. *Phys. Rev. Res.* **5**, 013035 (2023).
- [23] Hajr, A. *et al.* High-coherence kerr-cat qubit in 2d architecture. *Phys. Rev. X* **14**, 041049 (2024).
- [24] Réglade, U. *et al.* Quantum control of a cat qubit with bit-flip times exceeding ten seconds. *Nature* **629**, 778–783 (2024).
- [25] Grimm, A. *et al.* Stabilization and operation of a kerr-cat qubit. *Nature* **584**, 205–209 (2020).
- [26] Ni, Z. *et al.* Beating the break-even point with a discrete-variable-encoded logical qubit. *Nature* **616**, 56–60 (2023).
- [27] Grimsmo, A. L. & Puri, S. Quantum error correction with the gottesman-kitaev-preskill code. *PRX Quantum* **2**, 020101 (2021).
- [28] Lachance-Quirion, D. *et al.* Autonomous quantum error correction of gottesman-kitaev-preskill states. *Phys. Rev. Lett.* **132**, 150607 (2024).
- [29] Wang, C. *et al.* A schrödinger cat living in two boxes. *Science* **352**, 1087–1091 (2016).
- [30] Lescanne, R. *et al.* Exponential suppression of bit-flips in a qubit encoded in an oscillator. *Nat. Phys.* **16**, 509–513 (2020).
- [31] Gautier, R., Sarlette, A. & Mirrahimi, M. Combined dissipative and hamiltonian confinement of cat qubits. *PRX Quantum* **3**, 020339 (2022).
- [32] Bild, M. *et al.* Schrödinger cat states of a 16-microgram mechanical oscillator. *Science* **380**, 274–278 (2023).
- [33] Chávez-Carlos, J. *et al.* Spectral kissing and its dynamical consequences in the squeeze-driven kerr oscillator. *npj Quantum Inf.* **9**, 76 (2023).
- [34] Hillmann, T. & Quijandría, F. Quantum error correction with dissipatively stabilized squeezed-cat qubits. *Phys. Rev. A* **107**, 032423 (2023).

- [35] Nguyen, L. B. *et al.* Empowering a qudit-based quantum processor by traversing the dual bosonic ladder. *Nat. Commun.* **15**, 7117 (2024).
- [36] Pan, X. *et al.* Protecting the quantum interference of cat states by phase-space compression. *Phys. Rev. X* **13**, 021004 (2023).
- [37] Bhandari, B. *et al.* Symmetrically threaded squids as next generation kerr-cat qubits. *preprint arXiv:2405.11375* (2024).
- [38] Goto, H. Universal quantum computation with a nonlinear oscillator network. *Phys. Rev. A* **93**, 050301 (2016).
- [39] Guillaud, J. & Mirrahimi, M. Repetition cat qubits for fault-tolerant quantum computation. *Phys. Rev. X* **9**, 041053 (2019).
- [40] Puri, S. *et al.* Bias-preserving gates with stabilized cat qubits. *Sci. Adv.* **6**, eaay5901 (2020).
- [41] Iyama, D. *et al.* Observation and manipulation of quantum interference in a superconducting kerr parametric oscillator. *Nat. Commun.* **15**, 86 (2024).
- [42] Claes, J. & Puri, S. Estimating the bias of cx gates via character randomized benchmarking. *PRX Quantum* **4**, 010307 (2023).
- [43] Venkatraman, J., Cortiñas, R. G., Frattini, N. E., Xiao, X. & Devoret, M. H. A driven kerr oscillator with two-fold degeneracies for qubit protection. *PNAS* **121**, e2311241121 (2024).
- [44] Gravina, L., Minganti, F. & Savona, V. Critical schrödinger cat qubit. *PRX Quantum* **4**, 020337 (2023).
- [45] Ruiz, D., Gautier, R., Guillaud, J. & Mirrahimi, M. Two-photon driven kerr quantum oscillator with multiple spectral degeneracies. *Phys. Rev. A* **107**, 042407 (2023).
- [46] Carignan-Dugas, A., Wallman, J. J. & Emerson, J. Characterizing universal gate sets via dihedral benchmarking. *Phys. Rev. A* **92**, 060302 (2015).
- [47] Tacchino, F., Chiesa, A., Carretta, S. & Gerace, D. Quantum computers as universal quantum simulators: state-of-the-art and perspectives. *Adv. Quantum Technol.* **3**, 1900052 (2020).
- [48] Place, A. P. *et al.* New material platform for superconducting transmon qubits with coherence times exceeding 0.3 milliseconds. *Nat. Commun.* **12**, 1779 (2021).
- [49] Xu, Q., Iverson, J. K., Brandão, F. G. & Jiang, L. Engineering fast bias-preserving gates on stabilized cat qubits. *Phys. Rev. Res.* **4**, 013082 (2022).

- [50] Nguyen, L. B. *et al.* Programmable heisenberg interactions between floquet qubits. *Nat. Phys.* **20**, 240–246 (2024).
- [51] Hänggli, L., Heinze, M. & König, R. Enhanced noise resilience of the surface–gottesman-kitaev-preskill code via designed bias. *Phys. Rev. A* **102**, 052408 (2020).
- [52] Hoshi, D. *et al.* Entangling schrödinger’s cat states by bridging discrete-and continuous-variable encoding. *Nat. Commun.* **16**, 1–10 (2025).
- [53] Puri, S. *et al.* Stabilized cat in a driven nonlinear cavity: a fault-tolerant error syndrome detector. *Phys. Rev. X* **9**, 041009 (2019).
- [54] Ding, A. Z. *et al.* Quantum control of an oscillator with a kerr-cat qubit. *preprint arXiv:2407.10940* (2024).
- [55] Álvarez, P. *et al.* Biased ising model using two coupled kerr parametric oscillators with external force. *Phys. Rev. Lett.* **132**, 207401 (2024).
- [56] Goto, H., Lin, Z. & Nakamura, Y. Boltzmann sampling from the ising model using quantum heating of coupled nonlinear oscillators. *Sci. Rep.* **8**, 7154 (2018).
- [57] Yamaji, T. *et al.* Correlated oscillations in kerr parametric oscillators with tunable effective coupling. *Phys. Rev. Appl.* **20**, 014057 (2023).
- [58] Venkatraman, J., Xiao, X., Cortiñas, R. G. & Devoret, M. H. On the static effective lindbladian of the squeezed kerr oscillator. *preprint arXiv:2209.11193* (2022).
- [59] Ambegaokar, V. & Baratoff, A. Tunneling between superconductors. *Phys. Rev. Lett.* **10**, 486 (1963).
- [60] Steck, D. A. *Quantum and atom optics* (2007).
- [61] Krantz, P. *et al.* A quantum engineer’s guide to superconducting qubits. *Appl. Phys. Rev.* **6** (2019).
- [62] Kuroda, K. & Yuda, M. Niobium-stress influence on nb/al-oxide/nb josephson junctions. *J. Appl. Phys.* **63**, 2352–2357 (1988).
- [63] Lecocq, F. *et al.* Junction fabrication by shadow evaporation without a suspended bridge. *Nanotechnology* **22**, 315302 (2011).
- [64] Qing, B. *et al.* Broadband coplanar-waveguide-based impedance-transformed josephson parametric amplifier. *Phys. Rev. Res.* **6**, L012035 (2024).
- [65] Nielsen, E. *et al.* Gate set tomography. *Quantum* **5**, 557 (2021).

- [66] Brieger, R., Roth, I. & Kliesch, M. Compressive gate set tomography. *PRX quantum* **4**, 010325 (2023).
- [67] Cao, S. *et al.* Efficient characterization of qudit logical gates with gate set tomography using an error-free virtual z gate model. *Phys. Rev. Lett.* **133**, 120802 (2024).
- [68] Blume-Kohout, R. *et al.* Robust, self-consistent, closed-form tomography of quantum logic gates on a trapped ion qubit. *preprint arXiv:1310.4492* (2013).
- [69] Stemp, H. G. *et al.* Tomography of entangling two-qubit logic operations in exchange-coupled donor electron spin qubits. *Nat. Commun.* **15**, 8415 (2024).
- [70] Bartling, H. *et al.* Universal high-fidelity quantum gates for spin-qubits in diamond. *preprint arXiv:2403.10633* (2024).
- [71] Hashim, A. *et al.* Benchmarking quantum logic operations relative to thresholds for fault tolerance. *npj Quantum Inf.* **9**, 109 (2023).
- [72] Nielsen, E., Blume-Kohout, R. J., Rudinger, K. M., Proctor, T. J. & Saldty, L. Python gst implementation (pygsti) v. 0.9. Tech. Rep., Sandia National Lab.(SNL-NM), Albuquerque, NM (United States) (2019).
- [73] Nielsen, E., Blume-Kohout, R. J., Rudinger, K. M., Proctor, T. J. & Saldty, L. Python gst implementation (pygsti) v. 0.9. Tech. Rep., Sandia National Lab.(SNL-NM), Albuquerque, NM (United States) (2019).
- [74] Wille, R., Van Meter, R. & Naveh, Y. Ibm's qiskit tool chain: Working with and developing for real quantum computers (2019).
- [75] Blume-Kohout, R. *et al.* A taxonomy of small markovian errors. *PRX Quantum* **3**, 020335 (2022).
- [76] Carignan-Dugas, A., Ranu, S. K. & Dreher, P. Estimating coherent contributions to the error profile using cycle error reconstruction. *Quantum* **8**, 1367 (2024).

Acknowledgments

We are grateful to Chuanhong Liu, Ravi Naik and Trevor Chistolini for fruitful discussions on experiments. We thank Shruti Puri and Jahan Claes for insightful suggestions.

This work was supported by the U. S. Army Research Office under grant W911NF-22-1-0258.

Author contributions

B.Q., Ah.H. and K.W. led and organized the project. B.Q. fabricated the device, performed the measurement and analyzed the data. Ah.H. and G.K. designed the device. Ah.H, G.K., and L.B.N. set up the cryogenic apparatus. I.H. and B.B. performed the theoretical analysis. Ah.H., K.W., N.J., N.G. and N.F. assisted with the measurement. J.H. offered the GST circuit and analyzed the GST data. Ak.H. assisted with the GST data analysis. Z.P., L.C., Z.K., C.J., H.K., and K.L. assisted with the device fabrication. J.D., A.J., D.S. and I.S. supervised the project and offered necessary supports. B.Q., K.W. and L.B.N. wrote the manuscript with input from all authors.

Competing interests

There are no competing interests to declare.

Materials & Correspondence

Raw data, analysis code and numerical simulations are available from the corresponding author on reasonable request. Requests for materials should be addressed to B.Q.

Figure Legends

Fig. 1 Kerr-cat qubit Concepts. **a** SNAIL nonlinear oscillator circuit with frequency ω_Q , nonlinear factors g_3, g_4 and Kerr nonlinearity K , and its energy spectrum with wave-functions. **b** SNAIL oscillator pumped by a two-photon stabilization drive at $\omega_S = 2\omega_Q$, and the engineered pseudo-potential profile with its spectrum and wave-functions. **c** Pseudo-potential profile and its spectrum engineered by a red-detuned two-photon stabilization drive, where the excited states become degenerate. **d** Bloch sphere defined by the coherent states and their superpositions, where $|\pm Z\rangle = |\pm \alpha\rangle$, $|\pm X\rangle = |C_\alpha^\pm\rangle \propto |\alpha\rangle \pm |-\alpha\rangle$, $|\pm Y\rangle = |C_\alpha^{\pm i}\rangle \propto |\alpha\rangle \pm i|-\alpha\rangle$. **e** Pseudo-potential profile under a single-photon drive Ω at ω_Q for $Z(\theta)$ gates. **f** Pseudo-potential profile under a blue-detuned two-photon stabilization drive for the $X(\pi/2)$ gate.

Fig. 2 Initialization and lifetimes. **a** The sequence for KCQ initialization. **b** The evolution of the potential profiles and wave-functions during the initialization. **c** The numerical simulation of the KCQ state population transfer during the initialization. **d** The bit-flip lifetime T_z of resonant-KCQ and detuned-KCQ as a function of mean photon numbers. **e** The phase-flip lifetime T_y of resonant-KCQ and detuned-KCQ with various mean photon numbers. The error bar comes from fitting uncertainty, and the theory predictions of lifetimes are calculated by master-equation simulations illustrated in[37] and Methods Section 4.1.

Fig. 3 GST results. SPAM-free Pauli transfer matrices, process infidelities, diamond distances, stochastic Pauli errors and coherent Pauli errors for **a** resonant-KCQ $X(\pi/2)$ gate with 367-ns gate time, **b** resonant-KCQ $Z(\pi/2)$ gate with 70-ns gate

time, **c** detuned-KCQ $X(\pi/2)$ gate with 418-ns gate time and **d** detuned-KCQ $Z(\pi/2)$ gate with 70-ns gate time. The uncertainty represents the variance of the model fitting.

Fig. 4 DRB results. **a** The bit-flip p_{bit} and phase-flip p_{ph} error of resonant- and detuned-KCQ. The error bars are smaller than the marker size and therefore not plotted. **b** The noise bias and phase-flip error on the same plot with the fault-tolerant regime shaded in yellow. The error bars indicate the fitting uncertainty of the DRB survival probability.

Fig. 5 Detuned-KCQ ground state and its energy with $\Delta = 2K$. **a** The fractional deviation of the ground state energy estimated by the unperturbed Hamiltonian and perturbation theory. **b** The difference between the coherent state and the ground state of the detuned-KCQ Hamiltonian calculated by numerical diagonalization (ND) and perturbation theory (PT).

Fig. 6 Master equation simulation. **a** The coherent state lifetimes with different mean photon number and their master equation simulation taking different incoherent processes into account. **b** KCQ Hamiltonian spectrum with detuned two-photon stabilization drive. **c** The coherent state lifetimes with different detuning and their master equation simulation.

Fig. 7 KCQ initialization and gate calibration. **a** The sequence for calibrating $X(\pi/2)$ gate with 400- μs relaxation time in the initialization, and the measured $|\pm Z\rangle$ population oscillation. **b** The numerical simulation of the results above it. **c** The tunneling between the ground states when the relaxation time is long enough in the initialization. **d** The sequence for calibrating $Z(\theta)$ gates and the measured Chevron-like plot. **e** The numerical simulation of the results above it. **f** The energy levels of the SAIL nonlinear oscillator modified by the detuning. **g** The sequence for observing the excited states tunneling with 4- μs relaxation time in initialization, and the measured population oscillation. **h** The numerical simulation of the results above it. **i** The tunneling between the excited states when the relaxation time is short.

5 Supplementary

5.1 Measurement Hardware, Device Layout and Device Parameters

The Kerr-cat qubit is implemented on a planar superconducting circuit device. The equivalent circuit diagram of the device with the measurement wiring diagram is shown in Fig. 8a, and the false-color micrograph of the device chip is shown in Fig. 8b. The key component of the Kerr-cat qubit device, SAIL nonlinear oscillator (yellow), consists of two SAILS shunted by a coplanar capacitor, where each SAIL is formed by three large Josephson junctions connected in parallel with a small Josephson junction, as shown in Fig. 8c. A readout resonator (dark green) is capacitively coupled to the SAIL nonlinear oscillator with a dispersive shift χ to enable the quantum nondestruction readout of the Kerr-cat qubit, and a Purcell filter (light green) is introduced

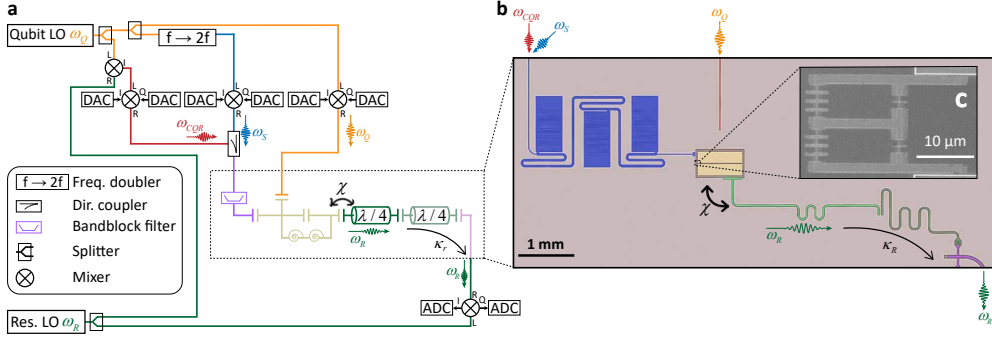


Fig. 8 Device and hardware. **a** Simplified wiring diagram of the chip and the measurement hardware, where the digital-to-analog converters (DACs) are implemented by an arbitrary waveform generator (AWG), and the analog-to-digital converters (ADCs) are implemented by an Alazar sampling card. **b** False-color micrograph of the Kerr-cat qubit device, where the SNAIL nonlinear resonator (yellow) is coupled to a readout resonator (dark green) with its Purcell filter (light green) for quantum nondemolition readout. A weakly coupled control port (orange) delivers the single-photon drive, and a strongly coupled pump port with a bandblock filter (purple) delivers the two-photon stabilization drive and cat-qubit readout drive with suppressed Purcell decay. **c** The scanning electron microscope picture of the two SNAILs.

between the readout resonator and the readout port (pink) to engineer the desired readout resonator decay rate κ_r with suppressed Purcell decay. We engineered two microwave ports to deliver the microwave efficiently without introducing too much Purcell decay. On the one hand, a control port (orange) is weakly coupled to the SNAIL nonlinear oscillator to deliver the single-photon drive for the continuous $Z(\theta)$ gates. On the other hand, a pump port (purple) with a bandblock filter is strongly coupled to the SNAIL nonlinear oscillator to deliver the two-photon stabilization drive and the cat-qubit readout (CQR) drive, where the bandblock filter strongly suppressed the Purcell decay from this port by blocking the signal around the qubit frequency. Detailed description of the bandblock filter can be found in our previous work[23].

We characterize the Kerr-cat qubit with the microwave network shown in Fig. 8a, where we neglect some filters, amplifiers and attenuators for simplicity and clarity, and a detailed wiring diagram can be found in our previous work[23]. The modulation and demodulation of the microwave drive is implemented by two local oscillators, frequency mixers, and a frequency doubler. A readout local oscillator (LO) at readout resonator frequency ω_R is introduced to demodulate the readout signal from the readout port (pink) of the device, and a qubit LO at SNAIL nonlinear oscillator frequency ω_Q is split into three parts to generate the control, readout and stabilization drives. The first one is directly fed into the IQ mixer to generate the single-photon drive, which is connected to the weakly coupled port (orange) of the device. The second one is fed into a frequency doubler to make its frequency doubled to $\omega_S \approx 2\omega_Q$ and generate the two-photon stabilization drive with the IQ mixer. Finally, the last one is mixed with the readout LO to generate the signal at the cat-qubit readout frequency $\omega_{CQR} \approx \omega_R - \omega_S/2$. The two-photon stabilization drive and the cat-qubit readout drive are both

connected to the strongly coupled port (purple) of the device through a directional coupler.

The parameters of the device and the calibration/estimation methods are described in Tab. 1.

Table 1 Device Parameters and Calibration Methods

Parameter	Value	Methods
SNAIL oscillator frequency ω_Q	$2\pi \times 5.9$ GHz	two-tone spectroscopy
SNAIL oscillator Kerr K	$2\pi \times 1.2$ MHz	two-tone spectroscopy
SNAIL large junction E_J	$2\pi \times 263.2$ GHz	room-temp. resistance msmt. [59]
SNAIL small-to-large junction ratio β	0.1	room-temp. resistance msmt. [59]
SNAIL oscillator charge energy E_c	$2\pi \times 118$ MHz	finite-element-method simulation
SNAIL oscillator relaxation time T_1	40 μ s	time-domain coherence msmt.
SNAIL oscillator dephasing time T_2	3.2 μ s	time-domain Ramsey msmt. [60]
Readout resonator frequency Ω_R	$2\pi \times 7.1$ GHz	microwave reflectrometry
Readout resonator relaxation rate κ_R	$2\pi \times 0.4$ MHz	microwave reflectrometry
Readout resonator dispersive shift χ	$2\pi \times 40$ kHz	time-domain spectroscopy

5.2 KCQ Hamiltonian Parameter Calibration

The KCQ Hamiltonian consists of three parameters: the detuning $\Delta = \omega_Q - \omega_S/2$, two-photon stabilization drive strength ϵ_2 and Kerr coefficient K . The parameters are extracted from a series of measurements. Without losing generality, we can set ϵ_2 to be real, and the two-photon stabilization drive frequency ω_S is known from the hardware.

We first extract the KCQ nonlinear oscillator parameters without the two-photon stabilization drive, i.e. $\epsilon_2 = 0$. The KCQ nonlinear oscillator frequency $\omega_Q = \omega_{01}$ is the transition frequency between $|0\rangle$ and $|1\rangle$, determined using standard two-tone spectroscopy[61]. The Kerr nonlinearity is then extracted by preparing the nonlinear oscillator in the first excited states $|1\rangle$ followed by a similar two-tone spectroscopy, where we observed two peaks corresponding to the $|1\rangle \rightarrow |0\rangle$ transition with frequency ω_{01} and $|1\rangle \rightarrow |2\rangle$ transition with frequency $\omega_{12} = \omega_{01} - 2K$, which allows us to extract the Kerr nonlinearity $K = 1.2$ MHz, as shown in Fig. 9a.

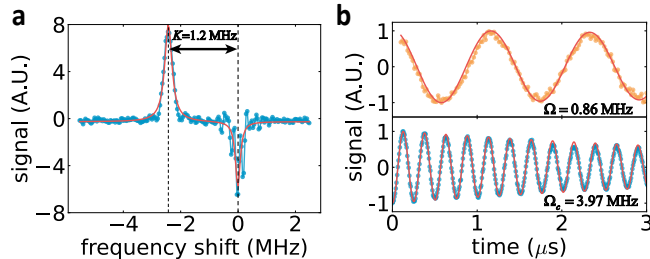


Fig. 9 KCQ Hamiltonian calibration. **a** Calibration of the Kerr nonlinearity. **b** Calibration of the two-photon stabilization drive.

Subsequently, we apply the two-photon stabilization drive to create cat states in the SNAIL nonlinear oscillator, and extract the value of ϵ_2 . With the two-photon stabilization drive, the KCQ Hamiltonian supports cat states $|C_\alpha^\pm\rangle \propto |+\alpha\rangle \pm |-\alpha\rangle$ with mean photon number $|\alpha|^2 = (\epsilon_2 + \Delta/2)/K$. Because K and Δ are already calibrated, we only need to calibrate $|\alpha|^2$. As mentioned in reference[23, 25], a single photon drive $H_d = \frac{\Omega}{2}\hat{a}^\dagger + \frac{\Omega^*}{2}\hat{a}$ induces a transition between the two cat states with the rate $\Omega_c = 2\text{Re}[\Omega]\alpha$ with $\epsilon_2 > 0$. Conversely, without the two-photon stabilization drive ($\epsilon_2 = 0$), the same drive can induce the transition between $|0\rangle$ and $|1\rangle$ states of the nonlinear oscillator with the rate Ω . Therefore, by tuning the phase of the single photon drive to make ϵ_1 real and measuring the two transition rates, we can extract, $\alpha = \Omega_c/(2\text{Re}[\Omega])$, as shown in Fig. 9b.

5.3 KCQ Hamiltonian and Eigenstates

The KCQ Hamiltonian is engineered through a superconducting nonlinear resonator under a strong two-photon stabilization drive. The SNAILs in the resonator provide the nonlinear potential

$$U_{\text{SNAIL}}(\phi) = -\beta E_J \cos \phi - 3E_J \cos \left(\frac{\phi_{\text{ext}} - \phi}{3} \right), \quad (7)$$

where $E_J/\hbar = 2\pi \times 263.2$ GHz is the Josephson energy of the large junction in SNAILs, $\beta = 0.1$ is Josephson energy ratio between the small and large junctions, ϕ_{ext} is the scaled external magnetic flux threading the SNAIL loop, and ϕ is the associated superconducting phase across each SNAIL.

For a fixed external flux, by Taylor expanding the potential energy up to the fourth order,

$$U_{\text{SNAIL}}(\phi) \approx U_{\text{SNAIL}}(\phi_{\text{min}}) + \sum_{k=2}^4 g_k (\phi - \phi_{\text{min}})^k, \quad (8)$$

one can observe that the SNAIL offers both non-zero third-order and fourth-order nonlinearities necessary for engineering the KCQ Hamiltonian. Under a two-photon stabilization drive, applying the rotating wave approximation in the rotating frame yields the effective Hamiltonian \hat{H}_{KCQ} shown in the main text. Without loss of generality, the two-photon stabilization drive will be assumed to be in-phase, i.e. $\epsilon_2 \in \mathbb{R}$.

To analyze the eigenenergy and eigenstates of this Hamiltonian, a displacement transformation $\hat{D}(\alpha)$ is introduced to obtain the corresponding Hamiltonian in the displacement frame written as

$$\hat{H}_{\text{KCQ}_{\text{disp}}} = E + \Lambda a^\dagger + \Lambda^* a + \tilde{\Delta} a^\dagger a + \tilde{\epsilon}_2 (a^{\dagger 2} + a^2) + \Gamma a^{\dagger 2} a + \Gamma^* a^\dagger a^2 - K a^{\dagger 2} a^2, \quad (9)$$

where the coefficients are given by

$$E = \Delta|\alpha|^2 - K|\alpha|^4 + \epsilon_2(\alpha^2 + \alpha^{*2}), \quad (10a)$$

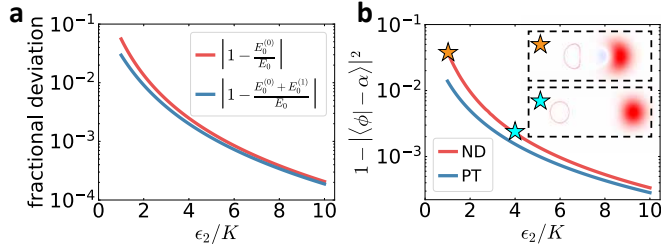


Fig. 10 Detuned-KCQ ground state and its energy with $\Delta = 2K$. **a** The fractional deviation of the ground state energy estimated by the unperturbed Hamiltonian and perturbation theory. **b** The difference between the coherent state and the ground state of the detuned-KCQ Hamiltonian calculated by numerical diagonalization (ND) and perturbation theory (PT).

$$\Lambda = -\Delta\alpha + 2K|\alpha|^2\alpha^* - 2\epsilon_2\alpha^*, \quad (10b)$$

$$\tilde{\Delta} = \Delta - 4K|\alpha|^2, \quad (10c)$$

$$\tilde{\epsilon}_2 = -K\alpha^2 + \epsilon_2, \quad (10d)$$

$$\Gamma = -2K\alpha. \quad (10e)$$

With a suitable choice of $\alpha = \sqrt{(\epsilon_2 + \Delta/2)/K}$, the single-photon drive terms are canceled out (i.e. $\Lambda = 0$), and the displaced Hamiltonian can be written as

$$\hat{H}_{\text{KCQ}_{\text{disp}}} = H_0 + H_1, \quad (11a)$$

$$H_0 = \frac{(\Delta/2 + \epsilon_2)^2}{K} - (4\epsilon_2 + \Delta) a^\dagger a, \quad (11b)$$

$$H_1 = -\frac{1}{2}\Delta(a^{\dagger 2} + a^2) - (2\epsilon_2 + \Delta)(a^{\dagger 2}a + a^{\dagger}a^2) - Ka^{\dagger 2}a^2, \quad (11c)$$

where the eigenstates and energies of H_0 are Fock states $|n\rangle$ with energy $E_n^{(0)} = (\Delta/2 + \epsilon_2)^2/K - (4\epsilon_2 + \Delta)n$, and H_1 is treated as a perturbation as long as its energy scale is much smaller than the energy gap of the unperturbed system ($|\epsilon_2| \gg |K|, |\Delta/2|$).

Firstly, the perturbed ground state energy is estimated as

$$\tilde{E}_0 = E_0^{(0)} + E_0^{(1)} + \dots = \frac{(\Delta/2 + \epsilon_2)^2}{K} + \frac{\Delta^2 K}{(4\epsilon_2 + \Delta)^2} + \dots, \quad (12)$$

As shown in Fig. 10, we plot the fractional deviation of the estimated ground state energy (\tilde{E}_0) from the exact ground state energy (E_0) given by the numerical diagonalization with various two-photon stabilization drive strength. In the regime of interest where $\Delta/K \sim 2$ and $\epsilon_2/K \sim 1-10$, the unperturbed ground state energy $E_0^{(0)}$ matches the exact ground state energy with less than 5% deviation, which is further improved slightly by the perturbation theory.

Secondly, the perturbed ground state (up to the first order) is given by

$$|\psi_0\rangle = \mathcal{N} \left(|0\rangle - \frac{\sqrt{2}\Delta}{4(4\epsilon_2 + \Delta)} |2\rangle \right), \quad (13)$$

where the perturbation introduces the occupation beyond the unperturbed ground states, and \mathcal{N} is the normalization factor. After returning to the undisplaced frame, the ground state ends up approximately to the coherent state shown in

$$|\phi\rangle = \hat{D}^\dagger(\alpha)|\psi_0\rangle = \mathcal{N} \left(|-\alpha\rangle - \frac{\sqrt{2}\Delta}{4(4\epsilon_2 + \Delta)} \hat{D}^\dagger(\alpha)|2\rangle \right) \approx |-\alpha\rangle. \quad (14)$$

The difference between the coherent state $|-\alpha\rangle$ and the ground state $|\phi\rangle$ of the detuned-KCQ when $\Delta = 2K$ is shown in Fig. 10. The Wigner functions of the ground states when $\epsilon_2/K = 1$ and $\epsilon_2/K = 4$ are also plotted in the inset indicated by the orange and blue stars. Both the results from perturbation theory and numerical diagonalization indicate the rapidly decreasing difference between the coherent state and the detuned-KCQ ground state. At the operating point in this work, such a difference is below 0.3%.

5.4 Device Fabrication

The device in this work is based on superconducting circuits patterned on an intrinsic silicon (Si) wafer with a resistivity $\rho \geq 10\text{k}\Omega \cdot \text{cm}$. The fabrication process is briefly depicted in the flow chart shown in Fig. 11a. Before the metal deposition, the wafer is cleaned by Piranha solutions ($\text{H}_2\text{SO}_4 + \text{H}_2\text{O}_2$) and hydrofluoric acid (HF) to remove the organic contamination and silicon oxide on the surface. The wafer is then transferred to a vacuum box to a Kert J. Lesker sputtering tool for niobium (Nb) deposition. By adjusting the sputtering temperature and pressure, a uniform niobium layer with compressive stress and high superconducting transition temperature[62] is sputtered onto the wafer. The superconducting transition temperature of the film is measured to be 8.94 K, as shown in Fig. 11b. The large structures, including the microwave buses, filter, quarter-wavelength resonators and capacitor pads, are patterned on the Nb film using photolithography and reactive ion etching (RIE). After a second cleaning process with HF to further remove oxides on Si and Nb surfaces, the Josephson junctions are defined with e-beam lithography (EBL) and bridge-free two-angle shadow evaporation of aluminum (Al) films[63]. Electrical contact between the Al Josephson junctions and the Nb capacitor pads is formed by the bandaid process with argon ion-milling[64]. Once diced, the device is packaged into a oxygen-free copper box for testing in the dilution refrigerator.

5.5 GST Circuit Design

GST is a self-consistent calibration free protocol for characterizing the noisy implementation of a informationally complete set of quantum gates[65–67]. GST can estimate the Pauli transfer matrix (PTM) of quantum gates in a SPAM-free manner, and is capable of fitting models with physical constraints such as completely positive, trace preserving (CPTP) constraints[65–67]. This technique has been applied to various platforms of quantum computing, including ion traps[68], spin qubits[69, 70] and

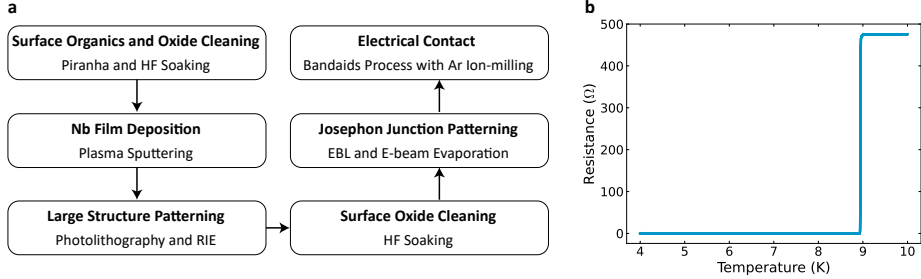


Fig. 11 Fabrication and film quality. **a** Flow chart of the device fabrication process. **b** Measurement of the superconducting transition temperature of the Nb film.

superconducting circuits[71]. GST usually executes a set of circuits that consist of a state preparation and readout sequence (*fiducials*) and repeated sequences of gate operations (*germs*) that amplify specific types of error [65, 72].

Because the local gates of KCQ are the discrete $X(\pi/2)$ gate and continuous $Z(\theta)$ gates, we construct the informationally complete set of quantum gates as $\{X(\pi/2), Z(\pi/2), Y(\pi/2)\}$, where the $Y(\pi/2)$ gate is compiled using local gates as $X(\pi)Z(\pi/2)X(\pi/2)Z(\pi/2)$. Each GST circuit has the form $F_iG^lF_j$, where F_i and F_j are *fiducial sequences*, G is a *germ* sequence, and l is the maximum integer such that the length of G^l is at most some maximum length L . Using the pyGSTi python package[73], we generate the GST circuits which have a germ set with 10 germs of maximum length 5. The fiducials and germs are shown in Tab. 2.

Table 2 Gate Set Tomography Germs and Fiducials

Germs	$Z(\pi/2), X(\pi/2), Y(\pi/2), Y(\pi/2)X(\pi/2), X(\pi/2)Z(\pi/2),$ $Y(\pi/2)Z(\pi/2), Y(\pi/2)X(\pi/2)X(\pi/2)Z(\pi/2),$ $Y(\pi/2)Y(\pi/2)Y(\pi/2)Z(\pi/2), X(\pi/2)Z(\pi/2)Y(\pi/2)Z(\pi/2)Z(\pi/2),$ $X(\pi/2)X(\pi/2)X(\pi/2)Z(\pi/2)$
Preparation Fiducials	$X(\pi/2), Y(\pi/2), X(\pi/2)X(\pi/2),$ no gates
Measurement Fiducials	$X(\pi/2), Y(\pi/2), X(\pi/2)X(\pi/2),$ no gates

We perform GST with 800 circuits of maximum lengths $L \in \{0, 1, 2, 4, 8, 16, 32, 64, 128\}$ and each circuit is implemented with 1024 shots to obtain the statistics of the measurement results. The process matrices and error generators of $X(\pi/2)$ and $Z(\pi/2)$ gates are extracted by fitting the measurement results to a model with CPTP constraints.

However, the uncertainty of the extracted Pauli X and Pauli Y errors from GST is very large due to the shallow depth of the GST circuits (128 at maximum), which hinders the exact characterization of the noise-bias. Therefore, we employ the DRB protocol with a maximum circuit depth of 2000 to explore the noise structure of KCQ and demonstrate that the performance of detuned-KCQ crosses the fault-tolerant threshold of the XZZX surface code[19, 42].

5.6 \mathbb{D}_8 Dihedral Group Randomized Benchmarking Design

The bit-flip error and phase-flip error, as well as the noise bias are extracted by the DRB protocol introduced in references[42, 46] with a scaling factor to compensate the effect of noise-free $X(\pi)$ gate. We will describe the protocol and illustrate the extraction of the scaling factor by numerical simulations.

The protocol consists of two modified RB sequences labeled by $b = 1$ and 2 , shown in Fig. 12a and Fig. 12b, which prepare and measure the qubit along Z and X axis, respectively. The random gates in RB sequences consist of a gate P sampled from the single qubit Pauli group \mathbb{P} , followed by n gates D_k sampled from the \mathbb{D}_8 dihedral group, and a final gate $D_{n+1} = (D_n \dots D_2 D_1)^{-1}$ to reverse the states. The bit-flip error and phase-flip error are extracted by fitting the character-weighted survival probability $S_b(n)$ (shown in Eq. 15) to an exponential function.

$$S_b(n) := \mathbb{E}_{\substack{P \in \mathbb{P} \\ U_1 \dots U_n \in \mathbb{D}_8}} [\chi_b^*(P) \Gamma_{\{U_i\}}] \quad (15)$$

Here, $\Gamma_{\{U_i\}}$ represents the expectation value of the measurement after applying a sample of RB sequences, while $\mathbb{E}[\cdot]$ denotes the average over all samples of gates. A few typical fitting plots are shown in Fig. 12c and Fig. 12d.

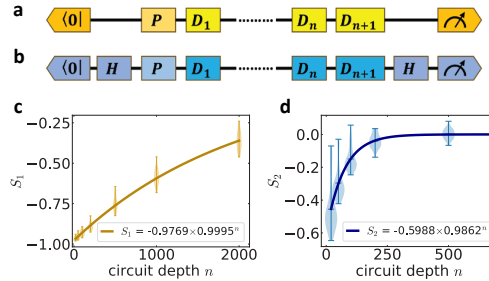


Fig. 12 DRB survival probability fitting. Circuits and fitting curve examples of the exponential decay in the \mathbb{D}_8 dihedral randomized benchmarking protocol when **a, c** preparing and measuring the states in Z axis, and **b, d** preparing and measuring the states in X axis.

The scaling factor between the errors of $Z(\theta)$ rotations and the extracted errors from DRB protocol is derived by numerical simulation with qiskit[74] package. We introduce various phase-flip errors $p_{\text{pf, real}}$ ranging from 0 to 3% and bit-flip errors $p_{\text{bf, real}} = 0.02p_{\text{pf, real}}$ to $Z(\theta)$ rotations, while keeping the $X(\pi)$ gate noise-free, and then simulate the DRB experiments to extract the bit-flip $p_{\text{pf, extracted}}$ and phase-flip errors $p_{\text{pf, extracted}}$. As shown in Fig. 13, the extracted errors are proportional to the errors on the $Z(\theta)$ rotations. By fitting the simulation results with a linear function, we extracted the scaling factor between them, where $p_{\text{pf, real}} = 1.02p_{\text{pf, extracted}}$ and $p_{\text{bf, real}} = 1.07p_{\text{bf, extracted}}$.

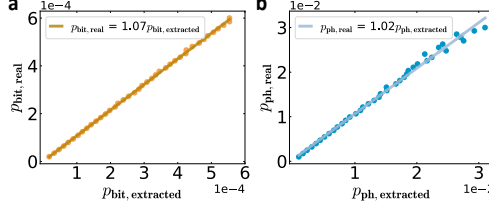


Fig. 13 Scaling factor **a** between the extracted and real bit-flip errors, and **b** between the extracted and real phase-flip errors

5.7 Description and Analysis of the Error Channels

We model the error channels of KCQ as a combination of coherent Pauli rotation errors and incoherent stochastic Pauli errors described by a Pauli transfer matrix $\mathcal{E} = e^{\mathbf{L}}$ with the generator $\mathbf{L} = h_x \mathbf{H}_x + h_y \mathbf{H}_y + h_z \mathbf{H}_z + p_x \mathbf{P}_x + p_y \mathbf{P}_y + p_z \mathbf{P}_z$. The coherent components in the error generator are defined in Eq. 16, and the incoherent components are defined in Eq. 17.[75, 76]

$$H_x = \begin{pmatrix} 0 & 0 & 0 & 0 \\ 0 & 0 & 0 & 0 \\ 0 & 0 & 0 & -1 \\ 0 & 0 & 1 & 0 \end{pmatrix}, H_y = \begin{pmatrix} 0 & 0 & 0 & 0 \\ 0 & 0 & 0 & 1 \\ 0 & 0 & 0 & 0 \\ 0 & -1 & 0 & 0 \end{pmatrix}, H_z = \begin{pmatrix} 0 & 0 & 0 & 0 \\ 0 & 0 & -1 & 0 \\ 0 & 1 & 0 & 0 \\ 0 & 0 & 0 & 0 \end{pmatrix} \quad (16)$$

$$P_x = \begin{pmatrix} 0 & 0 & 0 & 0 \\ 0 & 0 & 0 & 0 \\ 0 & 0 & -2 & 0 \\ 0 & 0 & 0 & -2 \end{pmatrix}, P_y = \begin{pmatrix} 0 & 0 & 0 & 0 \\ 0 & -2 & 0 & 0 \\ 0 & 0 & 0 & 0 \\ 0 & 0 & 0 & -2 \end{pmatrix}, P_z = \begin{pmatrix} 0 & 0 & 0 & 0 \\ 0 & -2 & 0 & 0 \\ 0 & 0 & -2 & 0 \\ 0 & 0 & 0 & 0 \end{pmatrix} \quad (17)$$

In the limit of small errors, we can expand the Pauli transfer matrix as $\mathcal{E} = 1 + \mathbf{L} + 0.5\mathbf{L}^2 + o(\mathbf{L}^3)$ in Eq. 18 up to $O(p_m), O(h_n^2)$ with $m, n \in \{x, y, z\}$ and $p = p_x + p_y + p_z$, as shown below

$$\begin{pmatrix} 0 & 0 & 0 & 0 \\ 0 & 1 - 2(p_y + p_z) - \frac{1}{2}(h_y^2 + h_z^2) & -h_z(1 + p) + h_x h_y & h_y(1 + p) + 2h_x h_z \\ 0 & h_z(1 + p) + h_x h_y & 1 - 2(p_x + p_z) - \frac{1}{2}(h_x^2 + h_z^2) & -h_x(1 + p) + h_y h_z \\ 0 & -h_y(1 + p) + h_x h_z & h_x(1 + p) + h_y h_z & 1 - 2(p_x + p_y) - \frac{1}{2}(h_x^2 + h_y^2) \end{pmatrix} \quad (18)$$

The coherent error manifests as the off-diagonal elements of the Pauli transfer matrix, which can be effectively removed by the Pauli twirling process. The Pauli twirling process randomly insert Pauli gates $P \in \mathbb{P}$ while compiling circuits, and all the Pauli gates can be executed with error-free virtual X gate, high-fidelity bias-preserving Z gate or their combination. Therefore, Pauli twirled error channels introduces minimal extra noise with preserved the noise-bias property, and are reported to be statistically the same as the full error channels in XZZX surface code[19].

The Pauli transfer matrix of the error process after Pauli twirling process reduced to that of a Pauli stochastic error channel shown in Eq. 19,

$$\mathcal{E} = \begin{pmatrix} 0 & 0 & 0 & 0 \\ 0 & 1 - 2(p'_y + p'_z) & 0 & 0 \\ 0 & 0 & 1 - 2(p'_x + p'_z) & 0 \\ 0 & 0 & 0 & 1 - 2(p'_x + p'_y) \end{pmatrix} \quad (19)$$

where the associated stochastic Pauli errors are $p'_m = p_m + 0.25h_m^2$, $m \in \{x, y, z\}$. Even with the highest coherent error rate, $h_x = 0.0038 \pm 0.002$, of the bias-preserving $Z(\pi/2)$ gate estimated from GST, the contribution of stochastic Pauli X error from this coherent error is $3.61 \times 10^{-6} \pm 3 \times 10^{-6}$, which is two orders of magnitude smaller than the stochastic Pauli X error. Therefore, the effects of coherent errors are negligible.